scientific reports

Check for updates

OPEN

Out-of-phase tropical Atlantic–eruptions over the Last Millennium in PMIP4/past1000 simulations

Laura Verona[1,2]✉, Myriam Khodri[2] & Ilana Wainer[1]

**The Atlantic Niño, a key mode of tropical Atlantic variability
South America and
Atlantic
poorly understood due to the short observational record. Using multi-model simulations of the past millennium, we show that January volcanic eruptions induce a tropical out-of-phase lagged response, with long-lasting El Niño-lik , followed by austral summer Niña-like cooling in the Atlantic. These responses are triggered independently, driven by persistent equatorial atmospheric wave activity resulting from the interplay between relative cooling over the Indian
underscore the role of volcanic forcing in modulating
modifying the associated precipitation patterns, and contributing to a more comprehensive view of tropical interbasin ocean-atmosphere interactions.**

Past sea surface temperature (SST) and hydroclimate fluctuations during the Last Millennium (LM, 850–1850 C.E.) present a wide range and amplitude, as revealed by proxy records[1,2], many aspects of which remain poorly understood[3]. Climate model simulations suggest that large volcanic eruptions explain a significant portion of low-frequency natural climate variability during the Common Era[4–6]. Explosive volcanic eruptions inject aerosols into the stratosphere, which reduce incoming solar radiation and cool the surface for a couple of years[7–9]. However, their interference with internal variability processes is less clear[10]. Both models and proxy records suggest an increased probability of a Pacific El Niño-like response within one to two years after eruptions[11–13]. Although evidence of an El Niño-like response from SST reconstructions remains debated[14,15], sea level pressure (SLP) anomalies reconstruction indicate a weakening of the Walker Circulation, also consistent with an El Niño response[16]. While much work has been devoted to improving our understanding of the volcanic forcing impacts on El Niño-Southern Oscillation (ENSO), the effects on the tropical Atlantic, including its potential interactions with other ocean basins, have not been established.

In particular, the Atlantic Niño, an equatorial zonal mode similar to the Pacific El Niño, explains a large part (∼30%) of the natural variability in the tropical Atlantic and arises primarily as a result of the Bjerknes feedback[17–19]. This mechanism involves strong interactions between atmospheric and oceanic processes, driving changes in the equatorial Atlantic SST[20–22] (Fig. S1). This complex SST-atmosphere coupling impacts the monsoon systems of the surrounding continents, influencing precipitation patterns[23–27] and the meridional displacement of the Intertropical Convergence Zone (ITCZ)[28–30]. In recent decades, the Atlantic Niño variance has decreased significantly due to a weakening of the Bjerknes feedback[29–31], a trend that is projected to continue under greenhouse warming scenarios[32,33]. The Atlantic Niño is also influenced by internal atmospheric processes linked to SST variability in other oceans[34–36].

The two-way interactions between the tropical Atlantic and ENSO have been extensively studied, yet their mechanisms and strength remain subject to debate due to observational uncertainties and persistent limitations in climate models[22,28,37–40]. While Atlantic Niño can modulate ENSO development by altering the Walker Circulation and triggering thermocline adjustments in the equatorial Pacific[22,38,41,42], its contributions are complex and state-dependent[43]. Its influence is modulated by factors such as the mean SST background state[44–48] and the ITCZ position[49], multidecadal variability processes[50], in addition to Atlantic and ENSO diversity[43,51,52].

[1]Oceanographic Institute of the University of São Paulo (IO/USP), São Paulo, Brazil. [2]LOCEAN/IPSL, Sorbonne University/IRD/CNRS/MNHN, Paris, France. ✉email: verona.laura@usp.br

Conversely, ENSO also impacts equatorial Atlantic variability. Multi-year Pacific La Niña events can trigger warming over the eastern equatorial Atlantic by extending the Pacific Walker Circulation into the basin[53]. Regardless of event duration, the seasonal phase-locking is essential for ENSO to induce opposite-signed events in the equatorial Atlantic[36]. However, this teleconnection is also highly state-dependent, strengthening under cold Pacific mean states with strong easterlies[54]. The interaction is further shaped by asymmetries between ENSO phases, with La Niña events enhancing equatorial Atlantic warming through intensified wind–SST coupling, while El Niño exerts a weaker suppressive effect[51]. Additional discrepancies arise from ENSO diversity, as central-Pacific and eastern-Pacific events have different influences on the Atlantic[55,56]. Together, these factors help explain the observed interannual inconsistency in Pacific–Atlantic teleconnections. Despite these findings, limited observational records constrain our understanding of Atlantic Niño-ENSO interactions, particularly under natural forcings such as volcanic eruptions.

The uncertainty surrounding monsoon responses to volcanic eruptions[57–60] underscores the complexities of the coupled land–ocean–atmosphere system. These intertwined processes further complicate the identification of internally and externally generated components[17,61,62]. Despite the known importance of the tropical Atlantic in modulating precipitation over South American and African monsoons[28,30,63,64], limited knowledge exists about its response to volcanic forcing, its interaction with other basins, and its contributions to tropical hydroclimate variability. Moreover, the limited observational period restricts our ability to fully characterize the natural variability spectra of the tropical Atlantic and possible future changes in its nature and frequency.

The LM is a valuable period for analyzing tropical Atlantic variability under natural forcing conditions, particularly due to the higher frequency and intensity of volcanic eruptions compared to the twentieth century[65] (Fig. 1a). Simulations from the Paleoclimate Modeling Intercomparison Project phase 4 (PMIP4/past1000)[66,67] show that Atlantic Niño consistently exhibits cooling following major eruptions, with sustained cooling evident after the thirteenth-century eruption cluster (as shown by the ATL3 index in Fig. 1b, see Methods section). These responses are reflected in significant power at multidecadal to centennial scales during the LM (Figs. 1c,d and S2), in contrast to the predominantly interannual-to-decadal variability observed in unforced pre-industrial control (piCtrl) simulations (Figs. 1e,f and S3). Isolating the intrinsic dynamics of the Atlantic Niño using relative SST anomalies (rSST), corresponding to the SST pattern changes relative to the mean tropical (20°N–20°) SST anomalies[11], suppresses volcanically induced radiative cooling, highlighting the dynamical component of Atlantic Niño response to volcanic forcing (3.5 to 4 years[17]). The LM residual Atlantic Niño exhibits potentially meaningful differences in integrated power spectra compared to piCtrl simulations (Fig. S4).

The distinct frequency content of the LM suggests that volcanic forcing may act as a pacemaker for Atlantic Niño variability, potentially modulating its intrinsic dynamics, although Atlantic Niño could also be modulated by the El Niño-like response in the Pacific through interbasin teleconnections. Here, we investigate this by analyzing tropical Atlantic variability during the LM relying on PMIP4/past1000 multi-model ensemble (MME). Through composites of strong tropical volcanic eruptions, we aim to uncover the mechanisms by which natural external forcing influence Atlantic Niño dynamics, ENSO interactions, and broader tropical climate variability. We explore volcanic eruption impacts on tropical surface heat budgets, atmospheric equatorial dynamics, and tropical oceans at the surface and subsurface.

Results and discussion

Out-of-phase Atlantic

To unfold the dynamical mechanisms of tropical Atlantic variability following large tropical eruptions during the LM, we rely on rSST and superposed epoch analysis (SEA)[68,69], an approach widely used for evaluating the climate impacts of volcanic events[12,14,16]. Our selection of eruptions is based on specific criteria concerning seasonality, ENSO preconditioning, and eruption location[10]. The composite includes only tropical eruptions, capturing radiative cooling that is mostly symmetric across the equator. Given the significant seasonal interplay in the Pacific–Atlantic atmospheric connection[36,70], we include only eruptions initiating during austral summer (December–January–February, DJF) and with radiative forcing peaking in austral winter (June–July–August, JJA, Fig. S5a,b). The double-peaked Samalas eruption (1257 A.D.) is excluded from the analysis to prevent contamination of the initial climate response by the secondary peak, facilitating comparison across events. The final selection includes 24 tropical eruptions (Fig. 1a).

We observe an out-of-phase response between the tropical Atlantic and Pacific following the eruption, with contrasting rSST anomalies in each basin (Fig. 2). Volcanic aerosols cause a significant decrease in net surface shortwave radiation across the tropics[8,71], along with a cold anomaly in the eastern equatorial Atlantic, which spreads zonally and peaks in January of the year after the eruption (Yr+1), resembling an Atlantic Niña-like pattern (Fig. 2a,b). This cooling signal decreases but persists through the end of Yr+1 with consistent strengthening of the easterly equatorial winds (Fig. 2c). At the same time, a warming spreads from west to east in the equatorial Pacific, like an El Niño pattern, and peaks between July of the eruption year (Yr0) and January of the second year (Yr+2). This pattern shows two peaks of warming, the first one during Yr0 preceding the cooling in the Atlantic and the second during Yr+1 after the Atlantic maximum cooling. The Pacific warming is consistent with a weakening of the easterly zonal winds (Fig. 2d,e). This agrees with previous results that show an increased probability of an El Niño-like response following eruptions[11,13,72] and the wind weakening characteristic of a less intense Walker Circulation[16].

From January to March of the eruption year, initial cooling is observed in the eastern Pacific (Fig. 2d). This contributes to negative wind anomalies in the eastern Pacific that could be a driver for the recharge oscillator mechanism[73], which favors heat accumulation in the western Pacific and its later displaced eastward, supporting the development of the El Niño-like anomaly from July Yr0. In the Atlantic, an initial cold anomaly develops during the usual Atlantic Niño season (JJA)[22,74] but remains confined to the eastern region. This confinement is likely linked to a zonal gradient in equatorial winds during this season, which reduces the westward extension

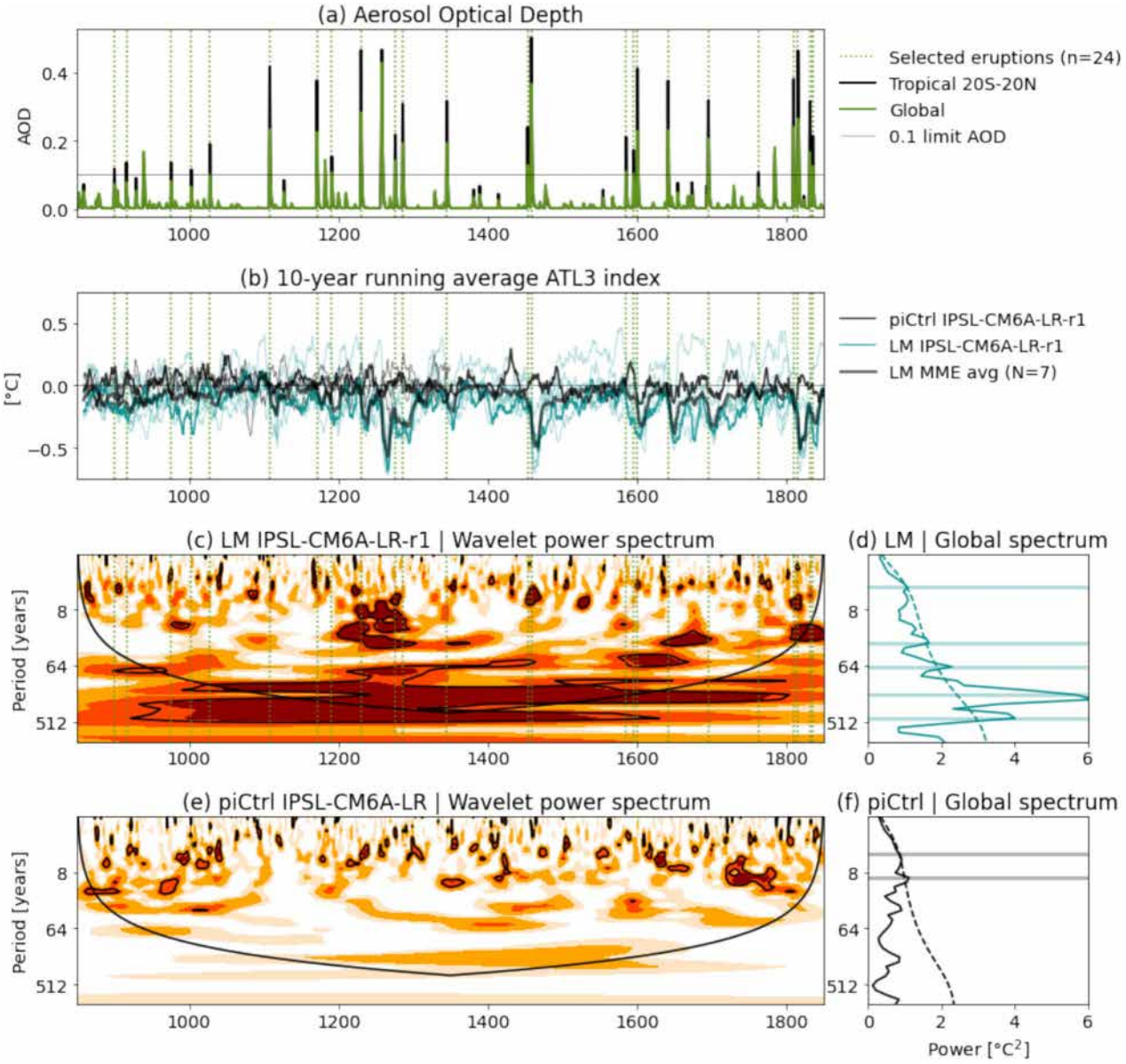

Fig. 1. IPSL-CM6A-LR Atlantic Niño index and frequency content. (**a**) Aerosol optical depth (AOD) time series for the past millennium (850–1850 C.E.). (**b**) 10-year running average ATL3 index computed with *full* SST anomalies. Thin blue lines represent the 7 PMIP4/past1000 MME members for the LM, the thick blue line is the IPSL-CM6A-LR-r1. The gray thick line is the MME average for the LM. Grey thin lines represent the 4 piCtrl simulations, the thick black line is the IPSL-CM6A-LR. The green dashed vertical lines are the selected eruptions from (**a**). Monthly ATL3 index wavelet power spectrum with black contours at 0.5, 1, 2, $4\,^{\circ}C^2$ for the IPSL-CM6A-LR-r1 (**c**) over the Last Millennium and (**e**) the unforced piCtrl simulation. (**d**) and (**f**) are the respective integrated power spectra with 95% confidence interval (dashed line) for the LM and piCtrl.

of the cooling. The wind gradient is associated with easterly wind anomalies appearing first from February to March of the eruption year along the equatorial Atlantic, followed soon after by westerly wind anomalies over the western Atlantic (Fig. 2c). Such equatorial wind anomalies are probably driven by the land-sea thermal contrast associated with the initial cooling of Africa from January to February of Yr0, further strengthened during the austral winter by the cooling of tropical South America (Fig. 4a).

During the second and third years following the eruption (Yr+2, Yr+3), the out-of-phase rSST signals persist, with the Pacific showing a negative anomaly while the Atlantic shows a positive rSST anomaly (Fig. 2b,d). In the Atlantic, the warming is more central and appears in austral winter (JJA), one season before the cooling in the preceding years. This warming suggests an Atlantic Niño-like structure peaking during its typical season[22]. The La Niña-like pattern in the second year after the eruption over the central Pacific has also been observed after the initial El Niño response following Pinatubo-like eruptions in CMIP6 models[59,72], though the Atlantic response has not been described. A recharge mechanism, frequently referenced for ENSO[73,75], may be at play in both

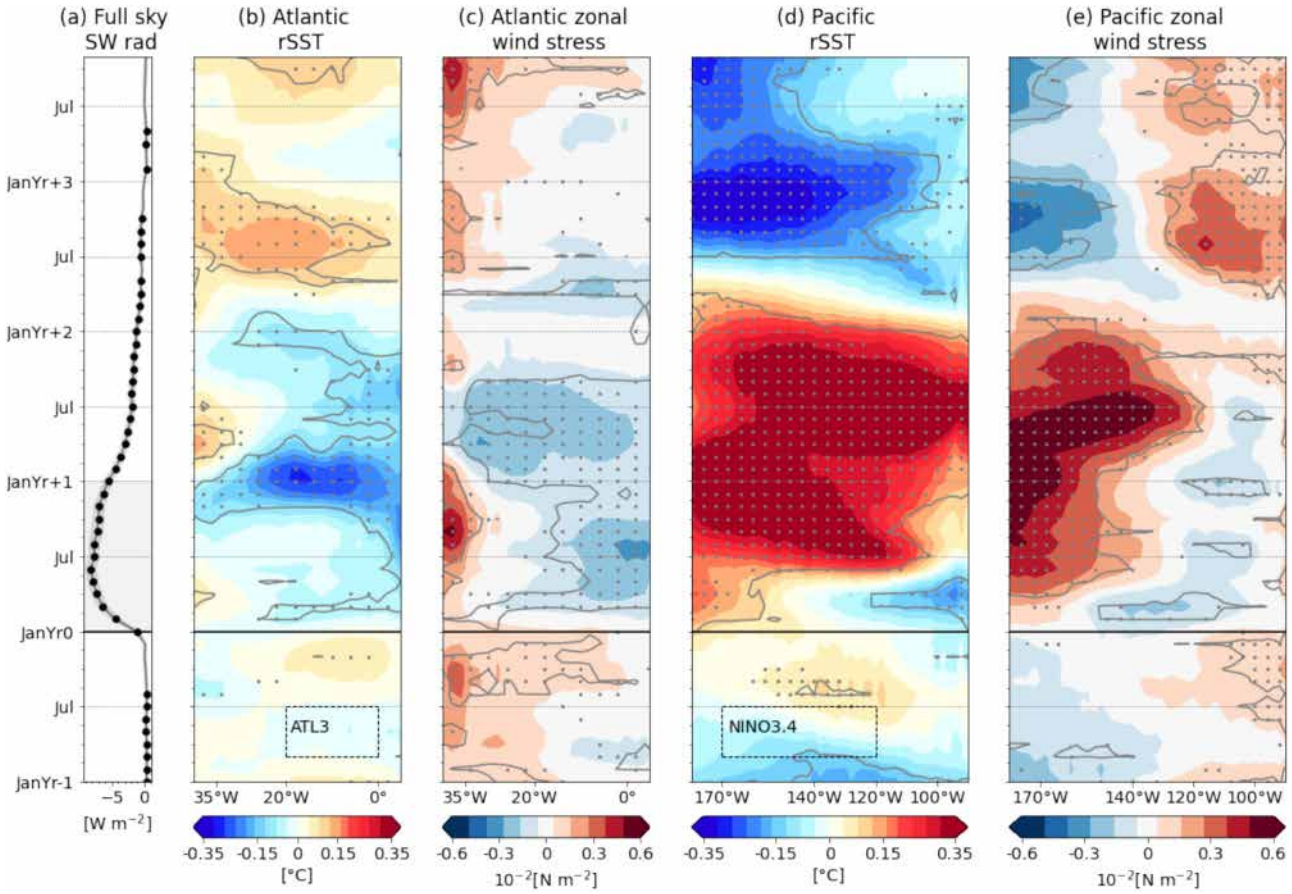

Fig. 2. Atlantic and Pacific response to Last Millennium January tropical eruptions. (**a**) Tropical full sky shortwave (SW) radiative flux. Longitude-time section for the latitudinal average between 5°N–5°S for the Atlantic (**b**) rSST, and (**c**) zonal wind stress. Same in (**e**) and (**d**) for the Pacific Ocean. Jan Yr0 represents the beginning of the eruption year. Stippling highlights times and locations where at least 60% (66/109) of the events display anomalies of the same sign. Gray contours correspond to the 95% significance level of anomalies according to a two-tailed Student's t-test.

oceans in the second year following the eruption. For instance, following the Atlantic Niña-like cooling signal, the reversed wind stress anomaly in Yr+2 (Fig. 2c) contributes to the recharging of equatorial heat content, transitioning the cooling pattern into a warming signal. The reversal of wind stress in Yr+2 could also reflect an atmospheric bridge response to warm equatorial Atlantic rSST anomalies during JJA, associated with an enhanced Walker Circulation that promotes subsidence and surface wind divergence over the central Pacific, thereby contributing to the onset of La Niña[41,76].

These findings suggest an out-of-phase response between the tropical Atlantic and Pacific basins following tropical eruptions. Existing studies highlight a complex and debated lead-lag relationship between ENSO and the Atlantic Niño under present-day climate conditions, which depends on factors such as the background mean state[42,44,50,53], pattern diversity[39,40], atmospheric modulation[47,49], and seasonal phase-locking[36]. While this typical connection has been explored, the influence of volcanic forcing on the ENSO-Atlantic Niño interaction remains unclear, particularly whether tropical eruptions amplify, dampen, or alter this connection. Does volcanic forcing establish new pathways of Pacific–Atlantic interaction? To address this, we next investigate the correlation of ENSO-ATL3 indices and its potential modulation by January tropical eruptions.

ENSO and ATL3 relationship

Building on the out-of-phase Atlantic–Pacific responses observed in the PMIP4/past1000 MME following January tropical eruptions, we examine the relationship between the NINO3.4 and ATL3 indices under unforced conditions (hereafter referred to as *typical conditions*) and volcanic-forced conditions (i.e., *LM post-eruption*). Typical conditions are defined using the unforced piCtrl composite of internally driven ENSO events (Fig. 3b), which serves as a baseline to compare with the LM post-eruption response (Fig. 3c). Our results reveal a consistent out-of-phase correlation between these indices, with significant (at 95% confidence level) negative correlation coefficients of r=−0.72 under typical conditions and r=−0.80 following volcanic forcing (Fig. 3a). This indicates that El Niño events (positive NINO3.4 index) are associated with Atlantic Niña conditions (negative ATL3 index).

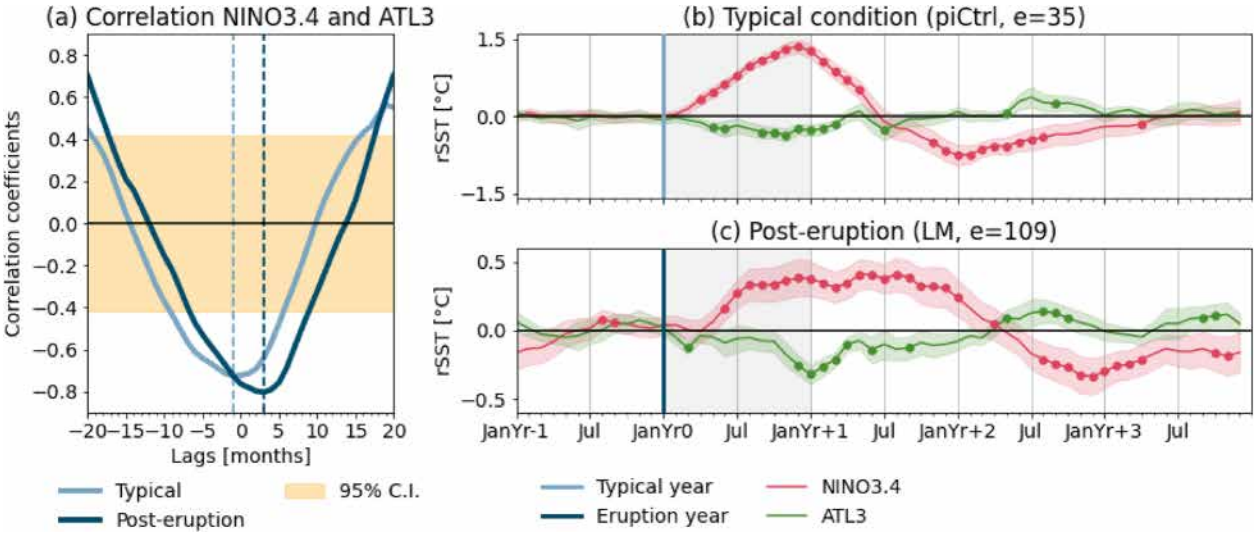

Fig. 3. ATL3 and NINO3.4 cross-correlations and superposed epoch composites. (**a**) Cross-correlation between NINO3.4 and ATL3 indices for typical conditions (light blue) and post-eruption (dark blue), the dashed lines correspond to the largest correlation coefficient for each case. Positive lag values, the NINO3.4 leads; and yellow shading represents the 95% confidence interval. Superposed epoch composites for ATL3 and NINO3.4 indices for (**b**) typical condition (piCtrl, 35 events) and (**c**) post-eruption (LM, 109 events). Dots indicate when most of the events display anomalies of the same sign, at least 68% (24/35) for (**b**) and 60% (66/109) for (**c**). The color shading indicates the events spreading, based on a 95% confidence interval from a two-tailed Student's t-test. The indices are computed using rSST anomalies.

To isolate the role of volcanic forcing in establishing the opposite-phase relationship between the Atlantic and Pacific, we focus on events that collectively yield a neutral ENSO precondition in the MME average (Fig. S5). This approach minimizes background ENSO variability, ensuring clearer correlations by selecting events that, while not individually neutral, result in average-neutral ENSO conditions across the ensemble for both LM (e=109) and piCtrl events (e=35). For instance, during years when DJF Pacific El Niño events are preceded by JJA Atlantic Niña, a negative correlation emerges, with the Atlantic initially playing a leading role. However, in most cases, Pacific El Niño events have already begun developing in the preceding JJA, ultimately placing the Pacific in a dominant role over the Atlantic[36]. Under typical conditions, Pacific El Niño events peak during DJF and decrease quickly, with an 85% probability of reaching a neutral-transitional state by March–April–May (MAM) of the following year (Figs. 3b and S7). In addition, there is about 83% probability of a negative rSST anomaly in the following year (Yr+2).

Simultaneously, the Atlantic shows a negative ATL3 index, consistent with an Atlantic Niña (Figs. 3b and S7). While the ATL3 signal is weaker than that of NINO3.4, it aligns for most MME events (dots in Fig. 3b), showing a 62% probability of occurrence during the first JJA, increasing to ∼77% during September–October–November (SON). The ATL3 index typically peaks in austral winter (JJA)[22]; however, our results show a negative signal that extends from June to the end of the year. This discrepancy may arise from inter-model diversity, which can present offsets in the ATL3 annual cycle or shifted peaks of variability, a common bias in CMIP6 models[29,77]. These biases influence the representation of the timing and magnitude of ATL3 variability across models, which is important when interpreting forced responses. Nevertheless, the persistence of a cold anomaly across most models, from May to the following March and peaking during SON, indicates that the MME average captures a coherent signal of equatorial Atlantic cooling (Fig. S6).

This negative correlation between the Pacific and Atlantic under typical conditions has previously been documented[36,53,55,78]. However, the lag between the two basins is highly dependent on background conditions and season locking of variability in each basin[36]. Our findings indicate that even though the Atlantic Niña peak is less pronounced than the Pacific El Niño, the negative 1-month lagged cross-correlation suggests that the Atlantic precedes the Pacific event (light blue line in Fig. 3a). However, this may be misleading, as under typical conditions the Atlantic wind anomaly develops only after the onset of the Pacific El Niño event (Fig. S6). El Niño-related wind anomalies typically emerge early in the year[36], with our results showing a significant central Pacific anomaly by March, while the Atlantic easterly wind anomaly is not triggered until June (Fig. S6). This atmospheric window from March to June facilitates strong atmosphere–ocean coupling between the two basins[36,70]. Conditions such as a shallower equatorial eastern Atlantic thermocline[79] and a near-equator position of the ITCZ[80] allow for the positive Bjerknes feedback from the Pacific to create an atmospheric bridge into the Atlantic. Additionally, the Atlantic wind anomaly initiates in the western region, suggesting an atmospheric bridge from the Pacific to the Atlantic via the Pacific-South America wave train[26,55].

This interconnected dynamic takes on added complexity under volcanic forcing. The post-eruption rSST signals in the Pacific and Atlantic differ from typical conditions, particularly regarding ENSO persistence and timing of events. In the Pacific, there is a 92% probability of a positive NINO3.4 anomaly occurring within the

first two years following the January tropical eruption (Figs. 3b and S7). Additionally, 73% of events initiate within the eruption year, with most beginning in the first semester. Thus, Pacific El Niño events usually peak in August of Yr0 and persist for approximately 1.5 years (Fig. 3b). Notably, 68% of post-eruption El Niño events last longer than 18 months, compared to 55% under typical conditions, while 35% persist beyond 24 months, in contrast to only 2% under typical conditions (Fig. S7).

The El Niño-like warming pattern observed in PMIP4/past1000 model experiments after tropical eruptions aligns with previous findings from model experiments and proxy reconstructions[11–13,75,81]. However, accounting for seasonality is essential when analyzing volcanic responses[10,82]. In this study, we focus on January tropical eruptions, with the radiative peak occurring during JJA as the NINO3.4 anomaly develops and reaches its peak in August with a long-lasting duration. In contrast, for June tropical eruptions, where radiative forcing peaks in DJF, the El Niño peaks during early austral summer (SON-DJF) of the following year[11,13].

Similarly to typical conditions, the post-eruption Atlantic shows a negative ATL3 response; distinctively, however, the peak tends to occur during the first DJF following the eruption, with a ∼73% probability. Importantly, the ATL3 relative cold anomaly lags by 3 months the initial peak of the Pacific El Niño in August (dark blue line in Fig. 3a). While previous studies have noted an Atlantic Niña-like response after June eruptions[11,13], the lagged relationship with Pacific El Niño and the triggering mechanisms have not been extensively discussed. Our findings suggest that the Atlantic Niña following the eruption only develops after the onset of a long-lasting Pacific El Niño-like warming. However, the Pacific El Niño initiates later in the year (JJA), missing the typical MAM seasonal window for a Pacific–Atlantic connection via an atmospheric bridge[36].

This raises the possibility that the DJF Atlantic Niña response to eruptions is driven by mechanisms other than the Pacific atmospheric bridge seen under typical conditions. Additional evidence from the Pinatubo ensemble experiment (29 members), which uses the IPSL-CM5B-LR model to simulate a June eruption under near-neutral ENSO preconditioning[11], supports this interpretation. An Atlantic Niña-like response emerges in DJF of the eruption year, even when the Pacific El Niño peak is delayed until JJA-SON of the following year (Fig. S8). Then, what drives the Atlantic Niña after eruptions? Could it be linked to the Pacific El Niño onset, or does volcanic forcing itself act as a pacemaker for tropical Atlantic variability by changing its intrinsic dynamics?

Seasonal tropical dynamics and interbasin interactions after January volcanic eruptions

To explore the mechanisms driving the response of the tropical Atlantic to January volcanic eruptions and its potential links to the Pacific dynamics, we now investigate the seasonal evolution of key climate components. This analysis focuses on the Walker Circulation, atmospheric equatorial dynamics, SLP and low-level (850 hPa) horizontal winds, land-sea temperature contrast, ocean surface and subsurface temperatures (Fig. 4), as well as associated precipitation anomalies (Fig. 5).

Eruption season (DJF Yr0) Africa is the first region to present significant cooling, with rSST anomalies at the 95% confidence level (Fig. S9). During this season, radiative cooling begins to penetrate below the surface in the Atlantic and Indian Oceans, whereas the Pacific Ocean behaves differently, showing no significant cooling. This interbasin configuration, combined with the land-sea temperature contrast, triggers an SLP anomaly characterized by a negative signal over the Pacific.

First post-eruption season (MAM Yr0): As radiative cooling intensifies during MAM, two distinct mechanisms emerge (Fig. 4a). First, an interbasin SLP dipole develops, driven by the relatively warmer Pacific and cooler regions over Africa, India, and the Indian Ocean. This configuration triggers a Gill-type response[83], characterized by eastward-propagating Kelvin waves (westerly wind anomaly) and westward-propagating Rossby waves (easterly wind anomaly). Previous studies using sensitivity experiments with CMIP5 models have identified this Gill response as a key driver of wind anomalies following June tropical eruptions[11,13,81]. Our analysis suggests that a similar mechanism might occur after January eruptions in the LM PMIP4/past1000 simulations. The relatively warmer western Pacific, combined with the westward wind anomaly from Kelvin waves, initiates the development of the Pacific El Niño-like pattern post-eruption.

This atmospheric wave activity is linked to reduced deep convection over the central Pacific, Africa, and Indonesia (Fig. 4a), leading to drier conditions in South America, equatorial Africa, and Indonesia during this season (Fig. 5b). Intensified drying in the Northern Hemisphere monsoon regions, such as Africa and India, has been documented from May to October following historical eruptions in the CMIP6 ensemble[59]. Similarly, large-ensemble climate sensitivity experiments show significant precipitation reductions across south and southeast Asia, associated with an El Niño-like response, Northern Hemisphere land cooling, and Indian Ocean cooling[84].

Under typical conditions, MAM is a key season for the Pacific–Atlantic Niños connection via an atmospheric bridge[36]. However, after January eruptions, this bridge from the Pacific to the Atlantic does not form because the Pacific El Niño is not yet significant. Instead, this window of strong atmospheric-ocean coupling, supported by a zonally aligned ITCZ over the equatorial oceans[36,53] (Fig. 5c), facilitates the Gill mechanism and the development of equatorial waves triggered by the initial cooling over Africa.

The second mechanism emerging during MAM involves an amplified zonal rSST gradient associated with eastward wind anomalies in the eastern Pacific and Atlantic boundaries (Figs. 4a and 2b,d). This gradient is short-lived and results from zonally asymmetric climatological low-level cloud feedbacks that translate uniform radiative forcing into uneven SST patterns[75]. In the Pacific, weak cooling in the eastern basin helps to maintain the rSST gradient, as seen following June eruptions like Pinatubo[11]. This pattern likely arises from the shallower mixed layer in the eastern compared to the central Pacific[59]. Additionally, the absence of a deeper-layer cooling signal suggests no development of a La Niña-like event (Fig. 4a). At higher latitudes, relative warming poleward of 15° is likely related to the continued confinement of the aerosol cloud within the equatorial region during this season[11]. The rSST anomalies in the equatorial Pacific drive wind anomalies that counteract Gill-induced winds, reflecting the complex interactions between SST and atmospheric dynamics during this season. In contrast, in the Atlantic, the zonal rSST gradient reinforces eastward wind anomalies generated by equatorial waves.

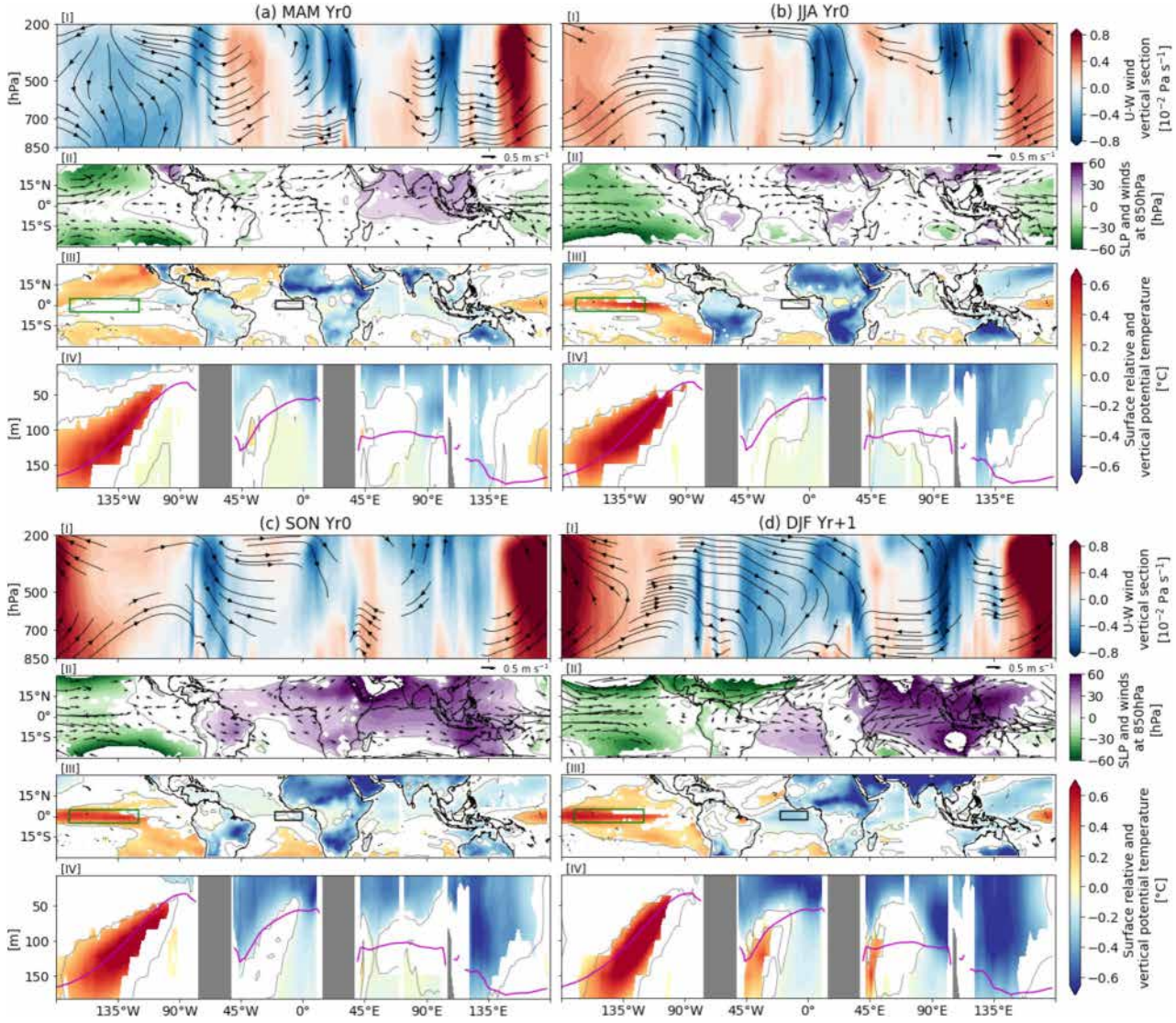

Fig. 4. Post-eruption seasonal evolution for tropical sections. (**a**) MAM Yr0. (**b**) JJA Yr0. (**c**) SON Yr0. (**d**) DJF Yr+1. Each panel shows [I] U-–5∘W anomaly 5°N–5°S cross-section average, the arrows are the significant vectors of the wind velocity anomalies. The vertical velocity is magnified by a factor of 100 to make its scale comparable to that of zonal wind. Shading represents the value of the pressure vertical velocity. [II] SLP in shading and arrows represent the low-level (850 hPa) horizontal wind anomalies. [III] Surface relative temperature, rTS over land and rSST over the oceans. [IV] Potential temperature anomaly 5°N-5°S cross-section average, magenta contours show the climatological 20°C isotherm (thermocline depth). For all panels, anomalies are only shown where at least 60% (66/109) of the events agree on sign. Gray contours correspond to the 95% significance level of the anomaly according to a two-tailed Student's t-test.

Volcanic radiative cooling in the eastern Atlantic penetrates deeper layers, particularly due to the shallower mixed layer in this portion of the basin (Fig. 4a).

Meanwhile, the Indian Ocean shows a faster and more integrated response to radiative cooling. Unlike the Pacific and Atlantic, where rSST changes might be more dynamically controlled, the Indian Ocean quickly integrates radiative cooling within the water column. This faster adjustment has been observed in volcanic forcing experiments, particularly in scenarios where aerosol forcing is concentrated over oceanic regions[85]. These contrasting responses across basins highlight the distinct roles of radiative cooling, rSST gradients, and atmospheric equatorial dynamics in shaping the tropical climate during this season.

Peak volcanic forcing and initial ENSO season (JJA Yr0): As radiative forcing peaks during JJA, we observe maximum cooling across all continents, particularly over Africa. This coincides with the seasonal ITCZ migration associated with the West African monsoon season (Figs. 4b and 5c). The intense cooling over Africa, along with associated drying, aligns with previous studies showing significant Sahel drying during the monsoon season (JJA) in the first two years after eruptions[59,86]. This drying is attributed to the pronounced land-sea thermal contrast over West Africa and the Pacific El Niño teleconnection, which induces widespread subsidence over

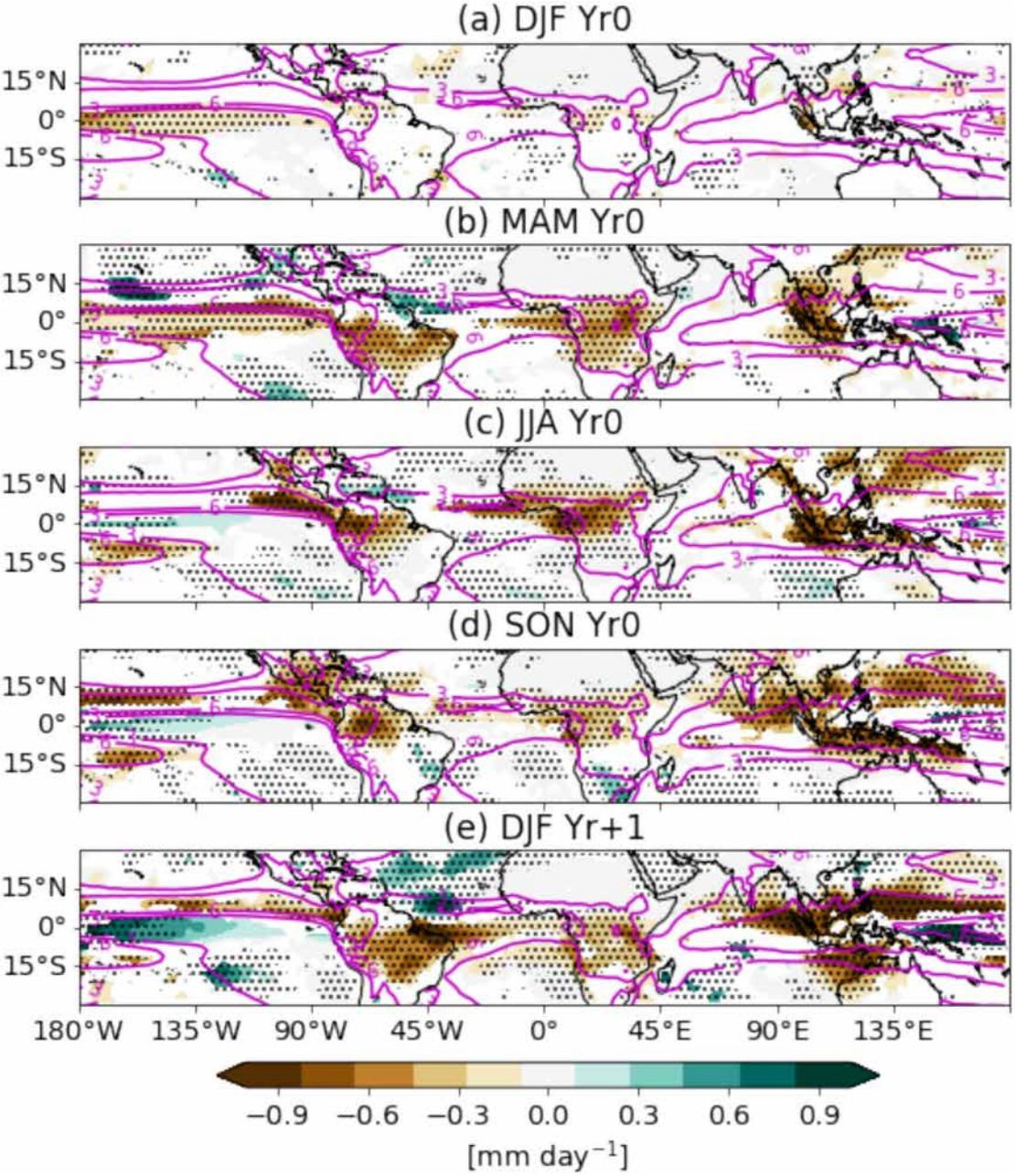

Fig. 5. Post-eruption seasonal evolution for tropical precipitation. From (**a**) to (**e**) DJF Yr0 to DJF Yr+1. Anomalies are only shown where at least 60% (66/109) of the events present the same sign. Stippling highlights locations where anomalies are significant at the 95% level according to a two-tailed Student's t-test. Magenta contours show the precipitation climatology in intervals of 3 mm day^{-1}.

the tropical Atlantic-Indian regions, a pattern also observed in our results (Fig. 4b). During the West African monsoon season, the enhanced cooling over Africa strengthens the positive SLP anomaly, driving low-level wind anomalies. Consequently, subsidence shifts from India to Africa, contributing to drier conditions[86] and sustaining the Gill mechanism.

In the Pacific, the relative warming initially observed in the western basin extends to the central Pacific, within the NINO3.4 region, triggering a significant positive NINO3.4 anomaly (Fig. 3b). This warming is further intensified by the surface outcropping of a warm subsurface anomaly (Fig. 4b). The combination of subsidence over Africa, an eastward shift of the downward wind anomaly from the central Pacific to the Americas, and an anomalous upward wind montion in the central Pacific aligns with the Walker Circulation weakening typical of El Niño conditions[16,87].

In the Atlantic, equatorial easterly winds gradually intensify, while volcanic-induced radiative cooling penetrates into the subsurface. This leads to the buildup of a cold anomaly above the equatorial thermocline (Fig.

4b). Therefore, the coupled atmospheric and oceanic responses established during JJA set the stage for further developments during the next transitional season.

Transitional season (SON Yr0): In the subsequent seasons, the interplay between the relative cooling over Africa, India, and the Indian Ocean continues to drive, individually or together, the SLP anomaly and, consequently, the equatorial wind anomalies. This is evident during SON (Fig. 4c), where a positive SLP anomaly persists over the colder regions, contrasting with the negative anomaly over the warmer Pacific, characteristic of an El Niño-like pattern.

Additionally, the Bjerknes positive feedback likely reinforces the initial rSST and wind anomalies in the Pacific[11,21]. Warming in the central and eastern Pacific further reduces the rSST gradient across the equatorial Pacific, weakening the trade winds. This weakening, in turn, reduces upwelling in the eastern Pacific, allowing warm surface waters to expand eastward and amplify the initial rSST anomaly. The weakened Walker Circulation, characterized by subsidence over Africa and the Indian Ocean and rising air over the central Pacific, sustains these conditions by reinforcing the eastward shift of convection. This leads to widespread drying across the equatorial region, except for the central Pacific, where increased precipitation reflects a typical El Niño response (Fig. 5d).

In the Atlantic, the relative cold anomaly in the eastern equatorial region spreads westward, following the enhanced easterly winds established in JJA (Fig. 4b,c). Within the upper 100 m, this radiative cooling is further advected westward by intensified zonal currents (Fig. 6a), associated with the westward-propagating climatological branches of the South Equatorial Current[88]. These processes contribute to the maturation of the Atlantic Niña-like pattern in the following season (Fig. 6b). Meanwhile, substantial cooling begins to develop in the subsurface of the western Indo-Pacific Ocean, indicating a gradual transition from an El Niño state toward a La Niña pattern.

Atlantic Niña peak season (DJF Yr+1): The Atlantic Niña reaches its peak during DJF, marked by the widespread cold anomalies across the equatorial Atlantic, with the strongest cooling concentrated in the ATL3 region (Figs. 4d, 3c, 6b). This culmination results from the subsurface recirculation of the radiative cooling anomaly within the thermocline, driven by stronger eastward currents below 100 m (Fig. 6a), associated with the climatological eastward-flowing Equatorial Undercurrent[89,90]. This aligns with previous findings that stronger Equatorial Undercurrent transport contributes to the development of negative SST anomalies in the eastern Atlantic, acting as an important positive feedback mechanism that reinforces the initial cold anomalies[89,91].

The combined effects of upwelling of cold water from below the thermocline and the zonal subsurface recirculation of volcanically induced cooling contribute to the persistence of the cold anomaly. Strengthened easterly winds further enhance upwelling, reinforcing the volcanic-triggered Atlantic Niña-like pattern. This sustained cooling significantly influences regional climate by altering atmospheric dynamics.

One major impact of the Atlantic Niña is its modulation of the ITCZ and precipitation over the surrounding continents. Although the ITCZ typically shifts southward during DJF, Figure 5 shows a pronounced dry anomaly south of Africa and over Northeast Brazil. This anomaly may be linked to a northward ITCZ shift induced by

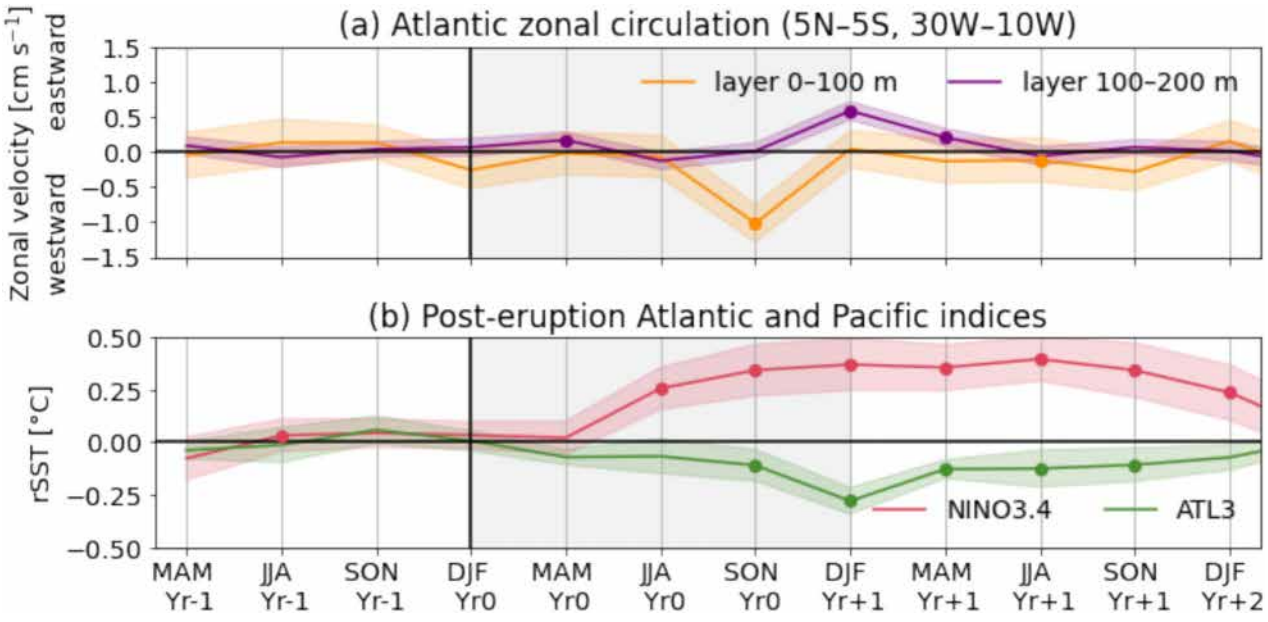

Fig. 6. Post-eruption Atlantic zonal currents, ATL3 and NINO3.4 indices. (**a**) Superposed epoch composites of seasonal zonal ocean currents averaged over the equatorial central Atlantic (5°N–5°S, 30°W–10°W) at two depth layers: 0–100 m (orange) and 100–200 m (purple). And (**b**) for NINO3.4 and ATL3 indices (LM, 109 events). Shading represents the 95% confidence interval based on a two-tailed Student's t-test, and dots indicate seasons where at least 60% of events (66/109) exhibit anomalies of the same sign. The indices are computed using rSST anomalies.

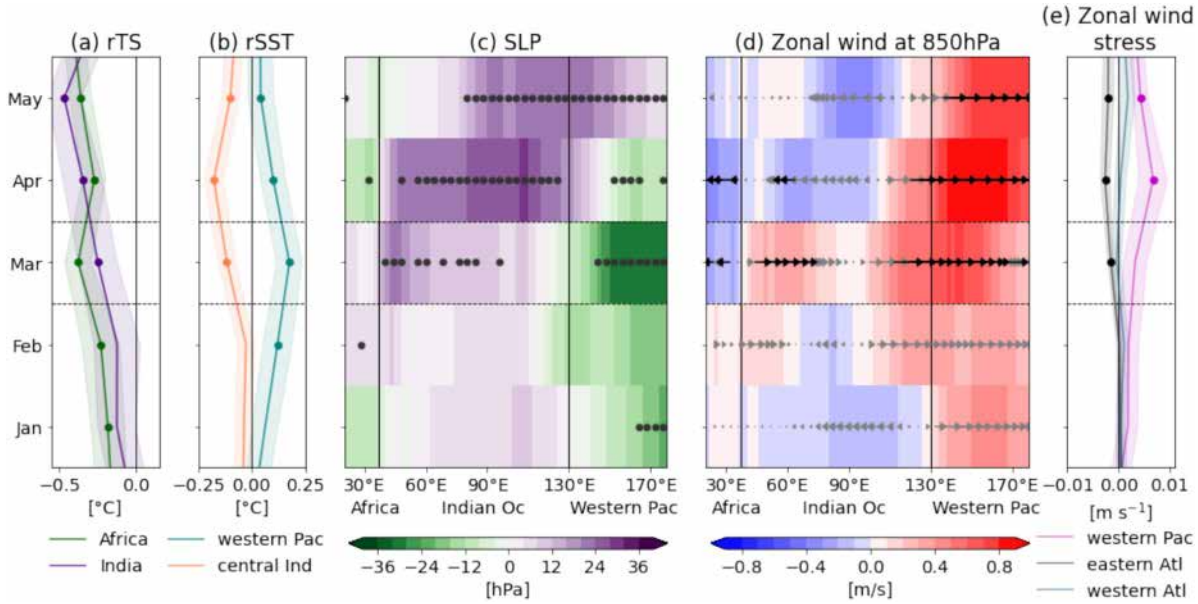

Fig. 7. Triggering mechanism after January tropical eruption. From January to May (**a**) rTS anomaly averaged over equatorial Africa (0°–25°N, 10°W–40°E) and India (10°N–30°N, 70°E–100°E). (**b**) rSST anomaly averaged for the western equatorial Pacific (5°N–5°S, 150°W–160°E) and central Indian (5°N–5°S, 50°E–90°E) basins. From Africa to western Pacific, the longitude-time section for the latitudinal average between 10°N–10°S for (**c**) SLP anomaly and (**d**) zonal wind velocity at 850 hPa, gray arrows show direction for the entire field, and black arrows where at least 60% of the events anomalies agree in sign. (**e**) Surface zonal wind stress anomaly for western equatorial Pacific (5°N–5°S, 140°E–170°E), eastern equatorial Atlantic (3°N–3°S, 10°W–0°), and western equatorial Atlantic (3°N–3°S, 45°W–25°W). For all panels, stippling and dots highlight times and locations where at least 60% (66/109) of the events display anomalies of the same sign and are significant at the 95% level according to a two-tailed Student's t-test.

the Atlantic Niña[28], disrupting typical seasonal rainfall patterns in these regions. These changes underscore the role of Atlantic Niña development in shaping equatorial atmospheric circulation during the post-eruption years.

Toward the end of the eruption year, a warm anomaly emerges in the tropical North Atlantic (Fig. 4d), potentially driven by ENSO teleconnections through multiple mechanisms. The Pacific El Niño enhances moist convection over the northern tropical Atlantic, increasing SST[92]. Additionally, increased precipitation in the western and central equatorial Pacific (Fig. 5e) activates the Pacific-North American pattern, weakening northeasterly winds over the northern tropical Atlantic[93] and contributing to positive SST anomalies. Further warming arises from heating over the Amazon, which influences the Atlantic Hadley Cell[94], weakening the northeasterly trade winds. A negative SLP anomaly further weakens these trades, amplifying warming through the Wind-Evaporation-SST feedback[95].

In addition to the Atlantic Niña effects, a drier South American monsoon season (DJF) is observed (Fig. 5e), associated with decreased monsoon winds over South America (Fig. 4d), likely driven by tropical North Atlantic warming in response to ENSO teleconnections[92]. This aligns with previous findings showing that global monsoon regions tend to dry after eruptions, particularly during DJF in the Southern Hemisphere[59]. The ongoing El Niño intensifies this drying[59], while the weakened monsoon feeds back into the El Niño pattern by relaxing Pacific trade winds. This feedback mechanism may contribute to the prolongation of the El Niño event[10].

The seasonal evolution of tropical dynamics following volcanic eruptions reveals a complex interplay of atmospheric circulation shifts, subsurface radiative cooling, and ocean-atmosphere interactions. The peak Pacific El Niño-like and lagged Atlantic Niña-like conditions are key drivers of tropical variability, significantly modifying the climate through changes in the wind and precipitation patterns. These processes highlight the distinct roles of individual basins and their interconnected responses in shaping the broader tropical climate during the post-eruption year.

While the impacts of these interactions are evident, understanding the underlying initial mechanisms that initially trigger these patterns is important. In the next section, we explore the specific atmospheric and oceanic processes initiated by January eruptions, focusing on the dynamics of the first months following the eruption.

Post-eruption triggering mechanisms

By examining the monthly evolution of key tropical climate processes, we identify the atmospheric and oceanic dynamics triggered by January tropical eruptions (Fig. 7), which ultimately lead to the development of an El Niño-like event in the Pacific and a lagged Niña-like pattern in the tropical Atlantic. The eruption response starts with a Gill-type mechanism in March. Due to their lower heat capacity, continents cool faster than the oceans[7],

with continental Africa showing the earliest signs of significant cooling in January (blue dots in Fig. 7a). At the same time, slight relative warming is observed over the western Pacific (Fig. 7b).

The cooling over Africa is not symmetrical, with equatorial regions cooling less than the off-equatorial areas due to the ITCZ position during March (Fig. S10a,b). Near the equator, collocated with the ITCZ position, a positive relative net surface heat flux (Fig. S11a), associated with reduced evaporation and decreased latent heat loss, moderates shortwave cooling. This effect is most pronounced over equatorial Africa, enhancing the temperature contrast with the off-equatorial regions. This enhanced contrast contributes to reduced equatorial Africa rainfall beginning in March and extending into the JJA monsoon season (Figs. 5a and S10b).

Although Africa is the first landmass to cool significantly after the eruption, in alignment with previous studies[11,13], the first low-level zonal wind anomalies occur in March, when the interbasin SLP dipole forms. This SLP dipole is triggered by peak cooling over Africa (Fig. 7a), alongside cooling over India and the Indian Ocean (Fig. 7a,b), in contrast to the relative warming over the western Pacific (Fig. 7b). These temperature gradients result in a positive SLP anomaly over the cooler regions and a negative SLP anomaly over the warmer Pacific (Fig. 7c,d). The source of atmospheric equatorial waves following tropical eruptions is still under debate[13], with some studies attributing it to equatorial Africa[11] and others to Southeast Asia[96]. Our results suggest that Africa plays the initial role; however, throughout the eruption year, this source shifts depending on the regions experiencing greater cooling, typically linked to changes in precipitation patterns.

The peak cooling over Africa, combined with reduced rainfall (Fig. 5a), is also associated with tropospheric heating[11]. This heating forces the Gill response, which drives an easterly wind anomaly to the west and a westerly wind anomaly to the east of the heat source[11,83] (Fig. 7d,e), due to the propagation of atmospheric Rossby and Kelvin waves (Fig. S11b). The interplay between cooling over the Indian Ocean and surrounding African and Indian continents, opposing the relatively warmer Pacific Ocean, sustains the basin-wise SLP seesaw. This mechanism drives equatorial wave activity, maintaining wind anomalies throughout the eruption year and generating the observed lagged out-of-phase Atlantic-Pacific responses (Fig. 4).

While this study focuses on January eruptions to isolate a seasonally coherent pathway, we acknowledge that the phasing between Pacific and Atlantic rSST responses is sensitive to the eruption timing due to seasonal phase locking. Using simulations from the June Pinatubo ensemble experiment[11], we verify the robustness of our findings beyond the January case, again observing a lagged out-of-phase response between the Atlantic and Pacific (Fig. S8). In this case, the ATL3 relative cold anomaly peaks during DJF Yr0, while the NINO3.4 warming peaks later on SON-DJF Yr+1. Despite the shift in timing, the Atlantic Niña response remains robust, indicating independent Atlantic and Pacific responses to the same volcanic forcing, each modulated by the seasonal positioning of the ITCZ, equatorial wave dynamics, and the intrinsic seasonality of each basin. This further reinforces the notion that volcanism acts as a pacemaker for the Atlantic Niña and Pacific Niño-like events, even for eruptions happening outside of January.

Concluding remarks

This study demonstrates that volcanic eruptions play an important role in shaping tropical Atlantic and Pacific climate variability by triggering distinct interbasin responses. Through analysis of the PMIP4/past1000 MME over the LM[66], we find that major tropical January eruptions generate significant El Niño-like warming in the Pacific, contrasting with a lagged Niña-like cooling response in the Atlantic. These out-of-phase lagged relative SST anomalies reveal that volcanic eruptions can modulate the interconnected tropical ocean-atmosphere interactions in ways not observed under typical, unforced conditions, suggesting that this natural forcing acts as an external component influencing tropical Atlantic–Pacific dynamics.

Our findings confirm that, while there is an unforced out-of-phase relationship between the ATL3 and ENSO indices, typically marked by a Pacific El Niño onset early in the year (February) leading to an Atlantic Niña in JJA-SON, via the optimal MAM seasonal window[36], and a peak in Pacific NINO3.4 warming in DJF, this response is significantly modified by volcanic events.

January eruptions, with radiative forcing peaking in austral winter, disrupt the typical Pacific-Atlantic atmospheric bridge due to the delayed ENSO onset (JJA), suggesting alternative mechanisms driving an Atlantic–Pacific out-of-phase lagged response under volcanic influence. Our results indicate that this lagged out-of-phase response is initially triggered by interbasin differential cooling over Africa, India, and Indian Ocean relative to the Pacific, which establishes a basin-wide SLP dipole and initiates a Gill-type atmospheric response. This mechanism drives equatorial Kelvin and Rossby waves, setting up westerly wind anomalies in the Pacific and easterly wind anomalies over the Atlantic.

The interplay between the relative cooling of the Indian Ocean and the surrounding continents (Africa and India), opposing the relatively warmer Pacific Ocean, drives the basin-wide SLP seesaw anomaly evolution, which sustains these atmospheric circulation patterns, contributing to the prolonged Pacific El Niño response (lasting up to 1.5 years) and the lagged Atlantic Niña response. This underscores the importance of equatorial wave dynamics and land-sea thermal contrasts in volcanic response mechanisms. Additionally, the subsurface recirculation of radiative cooling in the Atlantic appears essential for the full development of the Atlantic Niña-like pattern after eruption. This subsurface process explains both the 3-month lag after Pacific El Niño initial peak in August and the late DJF peak of the ATL3 index, which contrasts with the typical unforced Atlantic Niño events[19,22]. In addition, ENSO teleconnections may subsequently contribute to equatorial Atlantic wind anomalies, but the initial trigger for the Atlantic cooling originates from the Gill-type response to volcanic forcing.

Our results highlight the role of Gill-type equatorial wave responses in triggering the Pacific El Niño-like pattern after tropical eruptions in January, which was previously observed following June eruptions[11,13,81]. This mechanism also triggers the cold Atlantic Niña-like pattern, suggesting that the volcanic forcing acts as

a pacemaker for Atlantic Niño variability by modulating its intrinsic dynamics rather than only responding to volcanically-induced ENSO.

Our analysis focuses on January eruptions to isolate a specific seasonal pathway; however, we note that the relative timing between Pacific and Atlantic rSST responses is sensitive to the eruption timing due to seasonal phase locking. As such, the specific 3-month lagged out-of-phase relationship described here applies most directly to eruptions with radiative forcing peaking in JJA. Despite differences in phasing, complementary analyses of a June eruption ensemble indicates that the Atlantic Niña-like response occurs consistently, supporting the interpretation of independent Atlantic and Pacific responses to the same volcanic forcing. This confirms that volcanic forcing acts as a robust pacemaker modulating Atlantic variability across different eruption timings, with seasonal phase locking playing a key role in shaping the response. Therefore, emphasizing the importance of carefully considering seasonality and eruption characteristics when assessing volcanic impacts on climate.

Future research should expand this analysis using observations (instrumental and proxy records) and across a broader range of volcanic forcing scenarios, eruption timings, and background conditions. Overall, this study contributes to a more comprehensive view of tropical climate dynamics following eruptions, emphasizing the complex and interconnected nature of atmospheric and oceanic processes across basins. By examining past changes, it provides a historical framework for interpreting contemporary and future variations in tropical climate dynamics and their connections to the mean state.

Methods

PMIP4/past1000 Last Millennium simulations

This study uses the past millennium (850-1850, past1000[66]) simulations from the PMIP4[67] and the Coupled Model Intercomparison Project phase 6 (CMIP6)[97]. We employ available ensembles from IPSL-CM6A-LR[98,99], MPI-ESM1-2-LR[100,101], MRI-ESM2-0[102], and MIROC-ES2L[103,104]. This gives us seven ensemble members from four PMIP4/past1000 models (overview in Table S1). Pre-industrial control (piCtrl) simulations are used to calculate the climatology and quantify the internal climate variability.

The IPSL-CM6A-LR, MPI-ESM1-2, and MIROC-ES2L past millennium simulations include long-term volcanic forcing as aerosol optical depth (AOD) data from the evolv2k dataset[65] and produced by the Easy Volcanic Aerosol model[105]. The volcanic forcing from MRI-ESM2-0 is based on sulfur injection from evolv2k[65] and interacts with the MASINGAR aerosol chemical transport model[102]. Despite differences in volcanic forcing implementation in the MRI-ESM2-0 and MIROC-ES2L models, we include them to increase the sampling and diversity for the intercomparison of results across models.

Analysis and eruption selection

The ATL3 index, representing the Atlantic Niño, is estimated based on index-driven metrics as the SST anomaly averaged over 3°N–3°S, 20°W–0°[20]. We applied wavelet analysis[106] to the linearly detrended ATL3 index for each ensemble member to identify dominant frequencies that could be associated with volcanic forcing, in comparison with unforced piCtrl simulations.

The selection of volcanic events is a critical aspect of the analysis, as the response is influenced by numerous factors, including the spatiotemporal characteristics of the forcing and the preconditioning effects of the ENSO phase[14]. Strong tropical events are selected based on stratospheric AOD at 550 nm[60]. Tropical eruptions are defined when the mean AOD across 20°N–20°S exceeds the global mean AOD and the threshold of 0.1, comparable to a Pinatubo-like eruption (Fig. 1a). To avoid complications from double-peaked eruptions, only single-peak eruptions are included, resulting in 24 large tropical eruptions (Fig. S5). The radiative forcing magnitude is estimated as the global-mean anomaly of the full sky shortwave radiative flux at the top of the atmosphere. The first post-eruption year (Yr0) is then defined as the year with the maximum radiative forcing anomaly following the start of each selected eruption (Fig. S5b).

To ensure an ENSO-neutral precondition in the MME average prior to eruptions, we subsampled the initial event selection based on the NINO3.4 index, defined as the SST anomaly averaged over 5°N–5°S, 170°W–120°W[107]. For the year preceding the eruption (Yr-1), only individual events where the NINO3.4 remained within the ±1 standard deviation for the October–January average (the typical ENSO peak) are included. By applying this criterion to individual events, we ensure that the MME average remains ENSO-neutral, despite the fact that some events may deviate slightly from neutrality. Given the seasonality of the Atlantic Niño, we focused on eruptions occurring during DJF, with most beginning in January and, on average, radiative forcing peaking during JJA. This selection process results in 109 eruption events for the LM across all MME members (Fig. S5c).

After the classification of volcanic events, composites of different atmospheric and oceanic fields (SLP, ocean potential temperature, wind, and precipitation) are computed as mean anomalies relative to the climatology of each model piCtrl simulation. To ensure consistency across models, the climatology is calculated using the same 700-year period for all piCtrl runs, corresponding to the shortest available piCtrl simulation (MRI-ESM2-0, Table S1). Anomalies for all variables, including the NINO3.4 and ATL3 indices, are computed following the same procedure. To highlight SST gradients underlying the volcanic radiative cooling, we calculate relative SST (rSST) and surface air temperature over land (rTS) anomalies by removing the mean tropical (20°N–20°S) temperature anomaly from the temperature fields[10,11].

For comparison with the post-eruption signal, we selected typical El Niño events from unforced piCtrl simulations with DJF-averaged and standardized NINO3.4 index values greater than one standard deviation, ensuring neutral ENSO preconditioning in the MME average prior to El Niño events. This results in 35 El Niño events for the piCtrl.

A superposed epoch analysis (SEA)[68,69] is employed to analyze the median response to volcanic eruptions over a specified time interval. This method treats volcanic eruptions as replicate cases of the same process,

enabling an increased signal-to-noise ratio for a clearer understanding of the underlying response mechanisms. It is a widely used approach for evaluating the climatic impacts of volcanic events[11,12,14,16].

The statistical significance of the integrated power spectrum differences is assessed using the two-sample Kolmogorov–Smirnov test[108]. Linear relations between indices are quantified using Pearson's correlation coefficient[109]. All the correlations shown are statistically significant at the 95% confidence level, inferred from a t-test. The significance of anomalies is measured using a two-tailed Student's t-test (p-value<0.05) for each grid point, considering each model as an independent degree of freedom. Additionally, event agreement is used to assess the statistical significance of the observed changes, based on a binomial distribution with p=q=0.5. Thus, we assume that the probability that the sign of the change in each event is positive (p) or negative (q) is 0.5[11,110]. For the 109 LM composite events, the cumulative distribution function shows that a 60% event agreement (66 out of 109) indicates significance at the 99% level (Fig. S12). For piCtrl simulations, the same significance level is reached with 68% event agreement (24 out of 35). The consistency of the anomaly sign is a technique commonly used for analyzing CMIP models outputs, which helps to verify that statistically significant anomalies in the MME average accurately represent the ensemble members rather than being driven by outlier members.

Data availability

All PMIP4/CMIP6 datasets used in this study are publicly available at the Earth System Grid Federation via https://esgf-node.llnl.gov.

Code availability

The data analysis and figures presented in this article were conducted using Python. Codes are available upon request by contacting the corresponding author.

Received: 18 December 2024; Accepted: 11 November 2025
Published online: 08 December 2025

References

1. PAGES 2k Consortium. A global multiproxy database for temperature reconstructions of the Common Era. *Sci. Data.* **4**, 1–33. https://doi.org/10.1038/sdata.2017.88 (2017).
2. Steiger, N. J., Smerdon, J. E., Cook, E. R. & Cook, B. I. A reconstruction of global hydroclimate and dynamical variables over the common era. *Sci. Data* **5**, 1–15. https://doi.org/10.1038/sdata.2018.86 (2018).
3. Ljungqvist, F. C. et al. Northern hemisphere hydroclimate variability over the past twelve centuries. *Nature* **532**, 94–98. https://doi.org/10.1038/nature17418 (2016).
4. McGregor, H. V. et al. Robust global ocean cooling trend for the pre-industrial Common Era. *Nat. Geosci.* **8**, 671–677. https://doi.org/10.1038/ngeo2510 (2015).
5. Neukom, R., Steiger, N., Gómez-Navarro, J. J., Wang, J. & Werner, J. P. No evidence for globally coherent warm and cold periods over the preindustrial common era. *Nature* **571**, 550–554. https://doi.org/10.1038/s41586-019-1401-2 (2019).
6. Mann, M. E., Steinman, B. A., Brouillette, D. J. & Miller, S. K. Multidecadal climate oscillations during the past millennium driven by volcanic forcing. *Science* **371**, 1014–1019. https://doi.org/10.1126/science.abc5810 (2021).
7. Robock, A. Volcanic eruptions and climate. *Rev. Geophys.* **32**, 191–219 (2000).
8. Cole-Dai, J. Volcanoes and climate. *Wiley Interdiscipl. Rev. Clim. Change* **1**, 824–839. https://doi.org/10.1002/wcc.76 (2010).
9. Mignot, J., Khodri, M., Frankignoul, C. & Servonnat, J. Volcanic impact on the Atlantic Ocean over the last millennium. *Clim. Past* **7**, 1439–1455. https://doi.org/10.5194/cp-7-1439-2011 (2011).
10. Predybaylo, E., Stenchikov, G., Wittenberg, A. T. & Osipov, S. . El. niño/southern oscillation response to low-latitude volcanic eruptions depends on ocean pre-conditions and eruption timing. *Commun. Earth Environ.* **1**, 12. https://doi.org/10.1038/s43247-020-0013-y (2020).
11. Khodri, M. et al. Tropical explosive volcanic eruptions can trigger El Ninõ by cooling tropical Africa. *Nat. Commun.* **8**, 1–12. https://doi.org/10.1038/s41467-017-00755-6 (2017).
12. McGregor, S. et al. The effect of strong volcanic eruptions on enso. *El Niño Southern Oscillation in a Changing Climate*, 267–287. https://doi.org/10.1002/9781119548164.ch12 (2020).
13. Pausata, F. S., Zhao, Y., Zanchettin, D., Caballero, R. & Battisti, D. S. Revisiting the mechanisms of enso response to tropical volcanic eruptions. *Geophys. Res. Lett.* **50**, e2022GL102183. https://doi.org/10.1029/2022GL102183 (2023).
14. Zhu, F. et al. A re-appraisal of the enso response to volcanism with paleoclimate data assimilation. *Nat. Commun.* **13**, 747. https://doi.org/10.1038/s41467-022-28210-1 (2022).
15. Dee, S. G. et al. No consistent enso response to volcanic forcing over the last millennium. *Science* **367**, 1477–1481. https://doi.org/10.1126/science.aax2000 (2020).
16. Falster, G., Konecky, B., Coats, S. & Stevenson, S. Forced changes in the pacific walker circulation over the past millennium. *Nature* **622**, 93–100. https://doi.org/10.1038/s41586-023-06447-0 (2023).
17. Deser, C., Alexander, M. A., Xie, S.-P. & Phillips, A. S. Sea surface temperature variability: Patterns and mechanisms. *Ann. Rev. Mar. Sci.* **2**, 115–143. https://doi.org/10.1146/annurev-marine-120408-151453 (2010).
18. Deppenmeier, A. L., Haarsma, R. J. & Hazeleger, W. The Bjerknes Feedback in the Tropical Atlantic in CMIP5 models. *Clim. Dyn.* **47**, 2691–2707. https://doi.org/10.1007/s00382-016-2992-z (2016).
19. Dippe, T., Lübbecke, J. & Greatbatch, R. A comparison of the Atlantic and Pacific Bjerknes feedbacks: Seasonality, symmetry, and stationarity. *J. Geophys. Res. Oceans* **124**, 7442–7466. https://doi.org/10.1029/2018JC014700 (2019).
20. Zebiak, S. E. *Air–sea interaction in the equatorial Atlantic region*. https://doi.org/10.1175/1520-0442(1993)006< 1567 : $AIITEA$ >2.0.CO;2 (1993).
21. Bjerknes, J. Atmospheric teleconnections from the equatorial Pacific. *Monthly Weather Rev.* **97**, 163–172. https://doi.org/10.1175/1520-0493(1969)097<0163:ATFTEP>2.3.CO;2 (1969).
22. Keenlyside, N. S. & Latif, M. Understanding equatorial Atlantic interannual variability. *J. Clim.* **20**, 131–142. https://doi.org/10.1175/JCLI3992.1 (2007).
23. Folland, C. K., Colman, A. W., Rowell, D. P. & Davey, M. K. Predictability of northeast brazil rainfall and real-time forecast skill, 1987–98. *J. Clim.* **14**, 1937–1958. https://doi.org/10.1175/1520-0442(2001)014< 1937 : $PONBRA$ >2.0.CO;2 (2001).

24. Time-evolving sst modes related to west african rainfall. Polo, I., Rodríguez-Fonseca, B., Losada, T. & García-Serrano, J. Tropical atlantic variability modes (1979–2002). part i. *J. Clim.* **21**, 6457–6475. https://doi.org/10.1175/2008JCLI2607.1 (2008).
25. Losada, T. et al. A multi-model approach to the Atlantic Equatorial Mode: impact on the West African Monsoon. *Clim. Dyn.* **35**, 29–43. https://doi.org/10.1007/s00382-009-0625-5 (2010).
26. Lübbecke, J. F. et al. Equatorial Atlantic variabilityâ€: Modes, mechanisms, and global teleconnections. *Wiley Interdiscipl. Rev. Clim. Change* **9**, 1–18. https://doi.org/10.1002/wcc.527 (2018).
27. Vallès-Casanova, I., Lee, S.-K., Foltz, G. R. & Pelegrí, J. L. On the spatiotemporal diversity of atlantic niño and associated rainfall variability over West Africa and South America. *Geophys. Res. Lett.* **47**, e2020GL087108. https://doi.org/10.1029/2020GL087108 (2020).
28. Ruiz-Barradas, A., Carton, J. A. & Nigam, S. Structure of interannual-to-decadal climate variability in the tropical atlantic sector. *J. Clim.* **13**, 3285–3297. https://doi.org/10.1175/1520-0442(2000)013< $3285:SOITDC$ >2.0.CO;2 (2000).
29. Verona, L., Silva, P., Wainer, I. & Khodri, M. Weakened interannual tropical atlantic variability in cmip6 historical simulations. *Clim. Dyn.* **61**, 2797–2813. https://doi.org/10.1007/s00382-023-06696-9 (2023).
30. Tokinaga, H. & Xie, S. P. Weakening of the equatorial Atlantic cold tongue over the past six decades. *Nat. Geosci.* **4**, 222–226. https://doi.org/10.1038/ngeo1078 (2011).
31. Silva, P., Wainer, I. & Khodri, M. Changes in the equatorial mode of the Tropical Atlantic in terms of the Bjerknes Feedback Index. *Clim. Dyn.* **56**, 3005–3024. https://doi.org/10.1007/s00382-021-05627-w (2021).
32. Crespo, L. R. et al. Weakening of the atlantic niño variability under global warming. *Nat. Clim. Change* 1–6. https://doi.org/10.1038/s41558-022-01453-y (2022).
33. Yang, Y. et al. Suppressed atlantic niño/niña variability under greenhouse warming. *Nat. Clim. Change* 1–8. https://doi.org/10.1038/s41558-022-01444-z (2022).
34. Wang, C. Three-ocean interactions and climate variability: A review and perspective. *Clim. Dyn.* **53**, 5119–5136. https://doi.org/10.1007/s00382-019-04930-x (2019).
35. Zhang, L. & Han, W. Indian ocean dipole leads to atlantic niño. *Nat. Commun.* **12**, 5952. https://doi.org/10.1038/s41467-021-26223-w (2021).
36. Jiang, F. et al. Resolving the tropical Pacific/Atlantic interaction conundrum. *Geophys. Res. Lett.* **50**, e2023GL103777. https://doi.org/10.1029/2023GL103777 (2023).
37. Chang, P. et al. Climate fluctuations of tropical coupled systems—The role of ocean dynamics. *J. Clim.* **19**, 5122–5174. https://doi.org/10.1175/JCLI3903.1 (2006).
38. Ding, H., Keenlyside, N. S. & Latif, M. Impact of the equatorial Atlantic on the el niño southern oscillation. *Clim. Dyn.* **38**, 1965–1972. https://doi.org/10.1007/s00382-011-1097-y (2012).
39. Richter, I., Tokinaga, H., Kosaka, Y., Doi, T. & Kataoka, T. Revisiting the tropical Atlantic influence on el niño-southern oscillation. *J. Clim.* **34**, 8533–8548. https://doi.org/10.1175/JCLI-D-21-0088.1 (2021).
40. Zhang, L. et al. Emergence of the central Atlantic niño. *Sci. Adv.* **9**, eadi5507. https://doi.org/10.1126/sciadv.adi55 (2023).
41. Rodríguez-Fonseca, B. et al. Are atlantic niños enhancing Pacific enso events in recent decades? *Geophys. Res. Lett.* **36**. https://doi.org/10.1029/2009GL040048 (2009).
42. Cai, W. et al. Pantropical climate interactions. *Science*. **363**, eaav4236. https://doi.org/10.1126/science.aav4236 (2019).
43. Richter, I. et al. Comment on "resolving the tropical Pacific/Atlantic interaction conundrum" by feng jiang et al.(2023). *Geophys. Res. Lett.* **51**, e2024GL111563. https://doi.org/10.1029/2024GL111563 (2024).
44. Losada, T. & Rodríguez-Fonseca, B. Tropical atmospheric response to decadal changes in the Atlantic equatorial mode. *Clim. Dyn.* **47**, 1211–1224 (2016).
45. Wang, L., Yu, J.-Y. & Paek, H. Enhanced biennial variability in the Pacific due to Atlantic capacitor effect. *Nat. Commun.* **8**, 14887 (2017).
46. Jia, F. et al. Weakening Atlantic Niño–Pacific connection under greenhouse warming. *Sci. Adv.* **5**, eaax4111. https://doi.org/10.1126/sciadv.aax4111 (2019).
47. Svendsen, L., Rodríguez-Fonseca, B., Mohino, E., Crespo, L. & Losada, T. Tropical atmospheric response of Atlantic Niños to changes in the ocean background state. *Geophys. Res. Lett.***50**, e2023GL104332. https://doi.org/10.1029/2023GL104332 (2023).
48. Martín-Gómez, V., Rodríguez-Fonseca, B., Polo, I. & Martín-Rey, M. Observed global mean state changes modulating the collective influence of the tropical Atlantic and Indian oceans on ENSO. *J. Clim.* **37**, 3869–3886 (2024).
49. Losada, T., Rodríguez-Fonseca, B., Mechoso, C. R., Mohino, E. & Castaño-Tierno, A. Changes in interannual tropical Atlantic–Pacific basin interactions modulated by a south Atlantic cooling. *J. Clim.* **35**, 4403–4416 (2022).
50. Martín-Rey, M., Rodríguez-Fonseca, B., Polo, I. & Kucharski, F. On the Atlantic–Pacific Niños connection: A multidecadal modulated mode. *Clim. Dyn.* **43**, 3163–3178 (2014).
51. Jiang, L., Li, T. & Ham, Y.-G. Asymmetric impacts of El Niño and La Niña on equatorial Atlantic warming. *J. Clim.* **36**, 193–212 (2023).
52. Wang, R., He, J., Luo, J.-J. & Chen, L. Atlantic warming enhances the influence of Atlantic Niño on ENSO. *Geophys. Res. Lett.* **51**, e2023GL108013. https://doi.org/10.1029/2023GL108013 (2024).
53. Tokinaga, H., Richter, I. & Kosaka, Y. Enso influence on the atlantic niño, revisited: Multi-year versus single-year enso events. *J. Clim.* **32**, 4585–4600. https://doi.org/10.1175/JCLI-D-18-0683.1 (2019).
54. Richter, I. et al. Revisiting the inconsistent influence of El Niño-Southern Oscillation on the equatorial Atlantic. *J. Clim.* **38**, 481–496 (2025).
55. Rodrigues, R. R., Haarsma, R. J., Campos, E. J. & Ambrizzi, T. The impacts of inter-el niño variability on the tropical Atlantic and northeast Brazil climate. *J. Clim.* **24**, 3402–3422. https://doi.org/10.1175/2011JCLI3983.1 (2011).
56. Cai, W. et al. Changing El Niño-Southern oscillation in a warming climate. *Nat. Rev. Earth Environ.* **2**, 628–644 (2021).
57. Trenberth, K. E. & Dai, A. Effects of Mount Pinatubo volcanic eruption on the hydrological cycle as an analog of geoengineering. *Geophys. Res. Lett.* **34**, 1–5. https://doi.org/10.1029/2007GL030524 (2007).
58. Iles, C. E. & Hegerl, G. C. The global precipitation response to volcanic eruptions in the CMIP5 models. *Environ. Res. Lett.* **9**, https://doi.org/10.1088/1748-9326/9/10/104012 (2014).
59. Paik, S. et al. Determining the anthropogenic greenhouse gas contribution to the observed intensification of extreme precipitation. *Geophys. Res. Lett.* **47**, e2019GL086875. https://doi.org/10.1029/2019GL086875 (2020).
60. Villamayor, J. et al. Sahel droughts induced by large volcanic eruptions over the last millennium in pmip4/past1000 simulations. *Geophys. Res. Lett.* **50**, e2022GL101478. https://doi.org/10.1029/2022GL101478 (2023).
61. Bethke, I. et al. Norcpm1 and its contribution to cmip6 dcpp. *Geosci. Model Dev. Discuss.* 1–84. https://doi.org/10.5194/gmd-2021-91 (2021).
62. Hyun, S.-H., Yeh, S.-W., Kirtman, B. P. & An, S.-I. Internal climate variability in the present climate and the change in enso amplitude in future climate simulations. *Front. Clim.* **4**, 932978. https://doi.org/10.3389/fclim.2022.932978 (2022).
63. Carton, J. A., Cao, X., Giese, B. S. & Silva, A. M. D. Decadal and interannual SST variability in the tropical Atlantic Ocean. *J. Phys. Oceanogr.* **26**, 1165–1175. https://doi.org/10.1175/1520-0485(1996)026<1165:DAISVI>2.0.CO;2 (1996).
64. Giannini, A., Saravanan, R. & Chang, P. Oceanic forcing of sahel rainfall on interannual to interdecadal time scales. *Science* **302**, 1027–1030. https://doi.org/10.1126/science.1089357 (2003).
65. Toohey, M. & Sigl, M. Volcanic stratospheric sulfur injections and aerosol optical depth from 500 bce to 1900 ce. *Earth Syst. Sci. Data* **9**, 809–831. https://doi.org/10.5194/essd-9-809-2017 (2017).

66. Jungclaus, J. H. et al. The pmip4 contribution to cmip6-part 3: The last millennium, scientific objective, and experimental design for the pmip4 past1000 simulations. *Geosci. Model Dev.* **10**, 4005–4033. https://doi.org/10.5194/gmd-10-4005-2017 (2017).
67. Kageyama, M. et al. The pmip4 contribution to cmip6-part 1: Overview and over-arching analysis plan. *Geosci. Model Dev.* **11**, 1033–1057. https://doi.org/10.5194/gmd-11-1033-2018 (2018).
68. Rao, M. P. et al. A double bootstrap approach to superposed epoch analysis to evaluate response uncertainty. *Dendrochronologia* **55**, 119–124. https://doi.org/10.1016/j.dendro.2019.05.001 (2019).
69. Walton, S. D. & Murphy, K. R. Superposed epoch analysis using time-normalization: A python tool for statistical event analysis. *Front. Astron. Space Sci.* **9**, 1000145. https://doi.org/10.3389/fspas.2022.1000145 (2022).
70. Münnich, M. & Neelin, J. D. Seasonal influence of enso on the atlantic itcz and equatorial South America. *Geophys. Res. Lett.* **32**, https://doi.org/10.1029/2005GL023900 (2005).
71. Marshall, L. R. et al. Volcanic effects on climate: recent advances and future avenues. *Bull. Volcanol.* **84**, 1–14. https://doi.org/10.1007/s00445-022-01559-3 (2022).
72. Dogar, M. M. et al. A review of el niño southern oscillation linkage to strong volcanic eruptions and post-volcanic winter warming. *Earth Syst. Environ.* **7**, 15–42. https://doi.org/10.1007/s41748-022-00331-z (2023).
73. Jin, F.-F. An equatorial ocean recharge paradigm for enso. part i: Conceptual model. *J. Atmos. Sci.* **54**, 811–829. https://doi.org/10.1175/1520-0469(1997)054$<$ 0811 : $AEORPF$ $>$2.0.CO;2 (1997).
74. Richter, I. et al. Multiple causes of interannual sea surface temperature variability in the equatorial Atlantic Ocean. *Nat. Geosci.* **6**, 43. https://doi.org/10.1038/ngeo1660 (2013).
75. McGregor, S. & Timmermann, A. The effect of explosive tropical volcanism on ENSO. *J. Clim.* **24**, 2178–2191. https://doi.org/10.1175/2010JCLI3990.1 (2011).
76. Polo, I., Martin-Rey, M., Rodriguez-Fonseca, B., Kucharski, F. & Mechoso, C. R. Processes in the Pacific La Niña onset triggered by the Atlantic Niño. *Clim. Dyn.* **44**, 115–131 (2015).
77. Richter, I. & Tokinaga, H. An overview of the performance of cmip6 models in the tropical Atlantic: mean state, variability, and remote impacts. *Clim. Dyn.* **55**, 2579–2601. https://doi.org/10.1007/s00382-020-05409-w (2020).
78. Wang, C. An overlooked feature of tropical climate: Inter-Pacific–Atlantic variability. *Geophys. Res. Lett.* **33**, https://doi.org/10.1029/2006GL026324 (2006).
79. Richter, I. et al. Phase locking of equatorial Atlantic variability through the seasonal migration of the itcz. *Clim. Dyn.* **48**, 3615–3629. https://doi.org/10.1007/s00382-016-3289-y (2017).
80. Nnamchi, H. C., Latif, M., Keenlyside, N. S., Kjellsson, J. & Richter, I. Diabatic heating governs the seasonality of the Atlantic niño. *Nat. Commun.* **12**, 376. https://doi.org/10.1038/s41467-020-20452-1 (2021).
81. Liu, F. et al. Relative roles of land and ocean cooling in triggering an el niño following tropical volcanic eruptions. *Geophys. Res. Lett.* **49**, e2022GL100609. https://doi.org/10.1029/2022GL100609 (2022).
82. Stevenson, S., Fasullo, J. T., Otto-Bliesner, B. L., Tomas, R. A. & Gao, C. Role of eruption season in reconciling model and proxy responses to tropical volcanism. *Proc. Natl. Acad. Sci.* **114**, 201612505. https://doi.org/10.1073/pnas.1612505114 (2017).
83. Gill, A. E. Some simple solutions for heat-induced tropical circulation. *Q. J. R. Meteorol. Soc.* **106**, 447–462. https://doi.org/10.1002/qj.49710644905 (1980).
84. Singh, M. et al. Fingerprint of volcanic forcing on the enso–indian monsoon coupling. *Sci. Adv.* **6**, eaba8164. https://doi.org/10.1126/sciadv.aba8164 (2020).
85. Liu, F. et al. Tropical volcanism enhanced the east Asian summer monsoon during the last millennium. *Nat. Commun.* **13**, 3429. https://doi.org/10.1038/s41467-022-31108-7 (2022).
86. Villamayor, J., Ambrizzi, T. & Mohino, E. Influence of decadal sea surface temperature variability on northern brazil rainfall in cmip5 simulations. *Clim. Dyn.* **51**, 563–579. https://doi.org/10.1007/s00382-017-3941 (2018).
87. Janicot, S., Trzaska, S. & Poccard, I. Summer sahel-enso teleconnection and decadal time scale sst variations. *Clim. Dyn.* **18**, 303–320. https://doi.org/10.1007/s003820100172 (2001).
88. Stramma, L., Fischer, J., Brandt, P. & Schott, F. Circulation, variability and near-equatorial meridional flow in the central tropical Atlantic. *Elsevier Oceanogr. Ser.* **68**, 1–22 (2003) (**Elsevier**).
89. Brandt, P., Funk, A., Tantet, A., Johns, W. E. & Fischer, J. The Equatorial Undercurrent in the central Atlantic and its relation to tropical Atlantic variability. *Clim. Dyn.* **43**, 2985–2997. https://doi.org/10.1007/s00382-014-2061-4 (2014).
90. Brandt, P. et al. Atlantic equatorial undercurrent intensification counteracts warming-induced deoxygenation. *Nat. Geosci.* **14**, 278–282 (2021).
91. Góes, M. & Wainer, I. Equatorial currents transport changes for extreme warm and cold events in the Atlantic Ocean. *Geophys. Res. Lett.* **30**. https://doi.org/10.1029/2002GL015707 (2003).
92. Jiang, L. & Li, T. Relative roles of el niño-induced extratropical and tropical forcing in generating tropical north Atlantic (tna) sst anomaly. *Clim. Dyn.* **53**, 3791–3804. https://doi.org/10.1007/s00382-019-04748-7 (2019).
93. Enfield, D. B. & Mayer, D. A. Tropical Atlantic sea surface temperature variability and its relation to el niño-southern oscillation. *J. Geophys. Res. Oceans* **102**, 929–945. https://doi.org/10.1029/96JC03296 (1997).
94. Wang, C. ENSO, Atlantic climate variability, and the walker and Hadley circulations. *Hadley Circ. Present Past Future* **173**, 202 (2005).
95. Xie, S.-P. & Philander, S. G. H. A coupled ocean–atmosphere model of relevance to the itcz in the eastern pacific. *Tellus A* **46**, 340–350. https://doi.org/10.1034/j.1600-0870.1994.t01-1-00001.x (1994).
96. Chai, J. et al. A robust equatorial pacific westerly response to tropical volcanism in multiple models. *Clim. Dyn.* **55**, 3413–3429. https://doi.org/10.1007/s00382-020-05453-6 (2020).
97. Eyring, V. et al. Overview of the Coupled Model Intercomparison Project Phase 6 (CMIP6) experimental design and organization. *Geosci. Model Dev.* **9**, 1937–1958. https://doi.org/10.5194/gmd-9-1937-2016 (2016).
98. Boucher, O. et al. Presentation and evaluation of the ipsl-cm6a-lr climate model. *J. Adv. Model. Earth Syst.* **12**, e2019MS002010. https://doi.org/10.1029/2019MS002010 (2020).
99. Lurton, T. et al. Implementation of the cmip6 forcing data in the ipsl-cm6a-lr model. *J. Adv. Model. Earth Syst.* **12**, e2019MS001940. https://doi.org/10.1029/2019MS001940 (2020).
100. Mauritsen, T. et al. Developments in the mpi-m earth system model version 1.2 (mpi-esm1. 2) and its response to increasing co2. *J. Adv. Model. Earth Syst.* **11**, 998–1038. https://doi.org/10.1029/2018MS001400 (2019).
101. van Dijk, E., Jungclaus, J., Lorenz, S., Timmreck, C. & Krüger, K. Was there a volcanic-induced long-lasting cooling over the northern hemisphere in the mid-6th–7th century?. *Clim. Past* **18**, 1601–1623. https://doi.org/10.5194/cp-18-1601-2022 (2022).
102. Yukimoto, S. et al. The meteorological research institute earth system model version 2.0, mri-esm2. 0: Description and basic evaluation of the physical component. *J. Meteorol. Soci. Jpn. Ser. II.* **11**, 998–1038. https://doi.org/10.2151/jmsj.2019-051 (2019).
103. Hajima, T. et al. Development of the miroc-es2l earth system model and the evaluation of biogeochemical processes and feedbacks. *Geosci. Model Dev.* **13**, 2197–2244. https://doi.org/10.5194/gmd-13-2197-2020 (2020).
104. Ohgaito, R. et al. Pmip4 experiments using miroc-es2l earth system model. *Geosci. Model Dev.* **14**, 1195–1217. https://doi.org/10.5194/gmd-14-1195-2021 (2021).
105. an idealized forcing generator for climate simulations. Easy volcanic aerosol (eva v1. 0). *Geosci. Model Dev.* **9**, 4049–4070. https://doi.org/10.5194/gmd-9-4049-2016 (2016).
106. Torrence, C. & Compo, G. P. A practical guide to wavelet analysis. *Bull. Am. Meteorol. Soc.* **79**, 61–78. https://doi.org/10.1175/1520-0477(1998)079$<$ 0061 : $APGTWA$ $>$2.0.CO;2 (1998).

107. Trenberth, K. E. The definition of el nino. *Bull. Am. Meteorol. Soc.* **78**, 2771–2778. https://doi.org/10.1175/1520-0477(1997)078 $< 2771 : TDOENO >$2.0.CO;2 (1997).
108. Massey, F. J. Jr. The Kolmogorov–Smirnov test for goodness of fit. *J. Am. Stat. Assoc.* **46**, 68–78. https://doi.org/10.1080/01621459.1951.10500769 (1951).
109. Lee Rodgers, J. & Nicewander, W. A. Thirteen ways to look at the correlation coefficient. *Am. Stat.* **42**, 59–66. https://doi.org/10.1080/00031305.1988.10475524 (1988).
110. Pontes, G. M. et al. Drier tropical and subtropical southern hemisphere in the mid-pliocene warm period. *Sci. Rep.* **10**, 1–11. https://doi.org/10.1038/s41598-020-68884-5 (2020).

Acknowledgements

This study was supported by São Paulo Research Foundation (FAPESP) grants #2020/08490-0, #2022/11846-7, #2024/19122-3, #2020/14356-5; and CNPq.MCT.INCT.CRIOSFERA 408461/2024-1. Authors acknowledge support from the IPSL Climate Graduate School EUR and from the HPC resources of TGCC under grant no. A0150113826, A0160113826 and A0170113826 provided by GENCI (Grand Equipment National de Calcul Intensif). This study benefited from the ESPRI (Ensemble de Services Pour la Recherche l'IPSL) computing and data centre (https://mesocentre.ipsl.fr) which is supported by CNRS, Sorbonne Université, École Polytechnique and CNES.

Author contributions

L.V. performed the analysis, made the figures, and wrote the manuscript. L.V. and M.K. designed the study. M.K. discussed the methods, contributed to the interpretation of model results, and helped revise the manuscript. I.W. secured the financial resources that supported fellowships, travel, and data analysis, contributed to the study's conceptualization, and supervised the work. All the authors contributed with ideas, discussed the results, and contributed to improve the text.

Declarations

Competing interests

The authors declare no competing interests.

Additional information

Supplementary Information The online version contains supplementary material available at https://doi.org/10.1038/s41598-025-28495-4.

Correspondence and requests for materials should be addressed to L.V.

Reprints and permissions information is available at www.nature.com/reprints.

Publisher's note Springer Nature remains neutral with regard to jurisdictional claims in published maps and institutional affiliations.